Article

Magnesium Silicate Hydroxide−MoS$_2$−Sb$_2$O$_3$ Coating Nanomaterials for High-Temperature Superlubricity

Bin Wang, Kai Gao, Qiuying Chang, Diana Berman, and Yu Tian*

Cite This: *ACS Appl. Nano Mater.* 2021, 4, 7097−7106

Read Online

ACCESS | Metrics & More | Article Recommendations | SI Supporting Information

ABSTRACT: Expanding the low-friction temperature range of molybdenum disulfide-based coatings has been a topic of intense research interest. This paper introduces a coating concept, enabling achieving macroscale superlubricity, or near-zero friction, when exposed to open-air and high-temperature sliding conditions. This low-friction composite coating with a thickness of approximately 150−250 nm was accomplished by uniformly burnishing hydrothermally synthesized lamellate magnesium silicate hydroxide with an average diameter of 50 nm and an average thickness of 10 nm, molybdenum disulfide, and antimony trioxide powders onto a copper substrate. The tribological experiments performed in an open-air environment revealed that with the increase of testing temperature up to 200 °C or above (up to 300 or 400 °C), the coefficient of friction of the composite coating rapidly decreases and finally reaches the superlubricity state (the coefficient of friction is lower than 0.01). This intriguing superlubricity performance is attributed to the synergistic characteristics of lubricating antimony trioxide, molybdenum disulfide, and magnesium silicate hydroxide phases, enabling easy shearing of the film at high-temperature conditions. The results offer an approach for designing a solid lubricant solution for tribological applications.

KEYWORDS: magnesium silicate hydroxide, molybdenum disulfide, antimony trioxide, high temperature, macroscale superlubricity

MSH-Based Coating Nanomaterials
Interlayer Spacing
High-Temperature Superlubricity
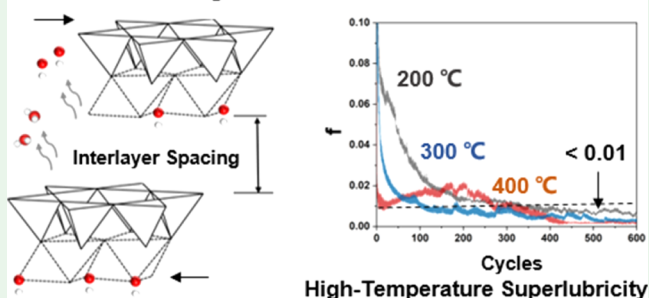
1. INTRODUCTION

Solid lubricant coatings are commonly used to improve the performance of systems operating under extreme pressure or high-temperature conditions.[1,2] With the rapid development of the aerospace industry, solid lubricant coatings are used under more extreme working conditions, including a relatively wide range of operating temperatures, atmospheric−vacuum irradiation, and multiple service environments. This resulted in the evolution of the coating design concepts——from the original single-phase solid lubricants [such as transition-metal dichalcogenides (TMDs),[3−5] soft metals,[6] fluorides,[7,8] and diamond-like carbon (DLC)[9,10]] to multiphase solid lubricants (such as PbO−MoS$_2$,[11,12] ZnO−WS$_2$,[13] and BaF$_2$/GaF$_2$−Ag−Cr$_3$C$_2$[14]) and adaptive nanocomposite coatings (also known as chameleon coatings, such as YSZ−Au−DLC−MoS$_2$,[15] Al$_2$O$_3$−DLC−Au−MoS$_2$,[16] and WC−DLC−WS$_2$[17]). Meanwhile, the synergetic effects of surface texturing and solid lubricants have been investigated.[18] Among the existing solid lubricants, TMDs, especially molybdenum disulfide (MoS$_2$), have become the most promising materials because of their excellent tribological properties in a vacuum environment.

For single-phase MoS$_2$ or MoS$_2$-based composite coatings, their strong covalent in-plane bonding combined with weak van der Waals interactions of the S−Mo−S planes (with a low shear strength of 1−2 MPa[19]) allow easy shearing and low friction at the substrate−coating−substrate interface.[1,2] The MoS$_2$ compound does not necessarily begin with its easy shearing (002) crystalline orientation planes that are parallel to the coating surface because the atomic planes self-arrange during the friction contact process.[1,3,19] The basal (002) plane surfaces of MoS$_2$ are less susceptible to oxidation and water adsorption than the (100) planes because of their higher chemical inertness.[20] Nevertheless, the preferential (002)-oriented planes of the crystalline MoS$_2$ coating lose substantial atomic layers when exposed to shearing under high-temperature (>350 °C) conditions owing to oxidation, which increases adhesive forces, reduces cohesive strength, introduces blisters, and generates relatively large wear debris.[1,2] The oxidized debris are pushed out of the sliding interface and do not adhere to the counterpart and shear, inhibiting the primary lubrication mechanisms. Correspondingly, to turn MoS$_2$-based coatings into a solid lubricant that can provide similar low-friction behavior at a wide range of temperature conditions,
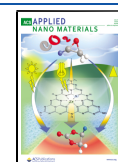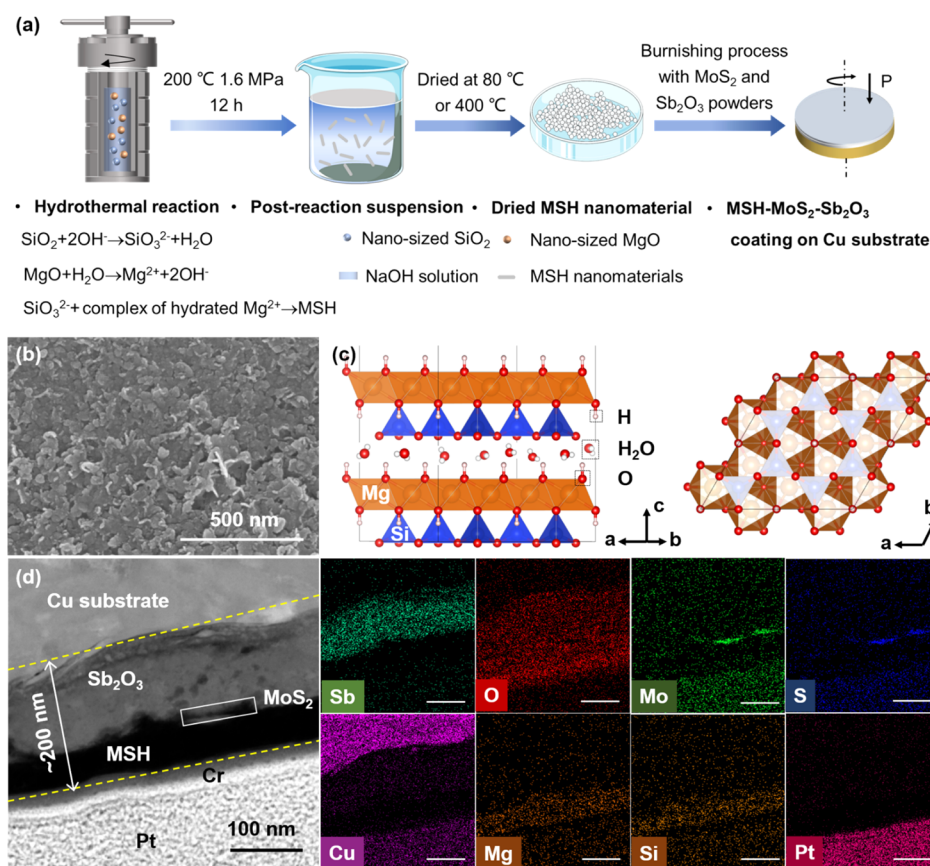
Figure 1. (a) Schematic diagrams of the hydrothermal synthesis of MSH nanomaterials and the burnishing of MSH−Sb$_2$O$_3$−MoS$_2$ composite coating. (b) Micromorphology and (c) structural diagram of hydrothermally synthesized MSH nanomaterials. (d) Cross-sectional morphology and elemental distribution maps of the as-prepared MSH−Sb$_2$O$_3$−MoS$_2$ composite coating. The scale bars shown in (d) are 100 nm. Cr and Pt protective layers were deposited to protect the coatings from damage during the TEM specimen preparation. TEM imaging caused some drift in the EDS elemental maps.

improving the tribological performance at high temperature has been intensely researched in the last few decades.

Based on the degradation mechanisms, most efforts to reduce the friction and wear and increase the lifetime of MoS$_2$-based coatings at high temperatures have focused on the alteration of MoS$_2$ surfaces for reduced oxygen and water adsorption. Binary or ternary doping materials, such as metals (titanium, aluminum, nickel, gold, chromium, vanadium, zirconium, and lead[21−26]), carbon-based materials,[27,28] antimony trioxide (Sb$_2$O$_3$),[21,29−36] and others,[37,38] have been proven to increase the coating density and hardness. Further, they act as thermal and oxygen diffusion barriers to improve the antioxidant characteristics of MoS$_2$-based coating. Among these doped materials, Sb$_2$O$_3$ has been valued for its outstanding synergistic effects with MoS$_2$. Hu et al.[32] first prepared multilayered MoS$_2$−Sb$_2$O$_3$ films via pulsed laser deposition and revealed that they have a much longer wear life than pure MoS$_2$ films in 40% RH air. They attributed the performance to the preservation of discharged fresh MoS$_2$ and the crack inhibition of Sb$_2$O$_3$ layers. Subsequently, Zabinski et al.,[33] Shirani et al.,[34] Lin et al.,[35] and Scharf et al.[36] performed detailed tribological studies on burnished or sputter-deposited Sb$_2$O$_3$−MoS$_2$−C and Sb$_2$O$_3$−MoS$_2$−Au composite coatings on stainless steel substrates and aluminum alloy modified by plasma electrolytic oxidation. The results showed that the wear suppression mechanisms of the Sb$_2$O$_3$ dopant in the MoS$_2$-based composite coating are associated with the reorganization

and enrichment of MoS$_2$, carbon, or gold lubricants at the topmost interface, providing a relatively strong basal support for the low-friction lubricants. Nevertheless, because a high-vacuum (or dry nitrogen atmosphere) and mild-temperature environment is a prerequisite for the low-friction MoS$_2$-based composite coating, its macroscale superlubricity in an open-air and high-temperature environment is rarely reported in the literature.

In this study, we prepared a magnesium silicate hydroxide−Sb$_2$O$_3$−MoS$_2$ (MSH−Sb$_2$O$_3$−MoS$_2$) composite coating by alternating burnishing of Sb$_2$O$_3$, MoS$_2$, and hydrothermally synthesized MSH nanopowders onto a polished copper substrate, and we demonstrated the superlubricity regime at elevated temperature conditions in an open-air system. MSH is a type of layered silicates that releases unsaturated Si−O−Si, O−Si−O, OH−Mg−OH (O), OH$^-$, and O−H−O groups, thus forming a tribofilm during the friction process.[39−42] It was previously reported that the high-temperature superlubricity phenomenon accomplished in a burnished MSH/C−Sb$_2$O$_3$ coating on a nickel superalloy substrate could be attributed to the formation of an easy shearing silicate-containing carbon film on the surface of the coating, which was tribochemically activated during sliding.[43] In this study, a MoS$_2$ lubricant was introduced as a replacement to the carbon lubricating phase, and the resulting synergistic superlubricity with the MSH nanomaterial and Sb$_2$O$_3$ was explored in an open-air and high-temperature system. This approach enabled the ultralow

Table 1. Mechanical Properties of the Copper Substrate and Burnished MSH−MoS$_2$−Sb$_2$O$_3$ Composite Coating

samples	roughness Ra (μm)	Young's modulus (GPa)	hardness (GPa)	thickness (μm)
Cu substrate	0.013 ± 0.003	127.97 ± 2.35	2.54 ± 0.05	N. A.
MSH−MoS$_2$−Sb$_2$O$_3$ coatings	0.258 ± 0.025	79.43 ± 8.02	1.62 ± 0.26	∼0.2
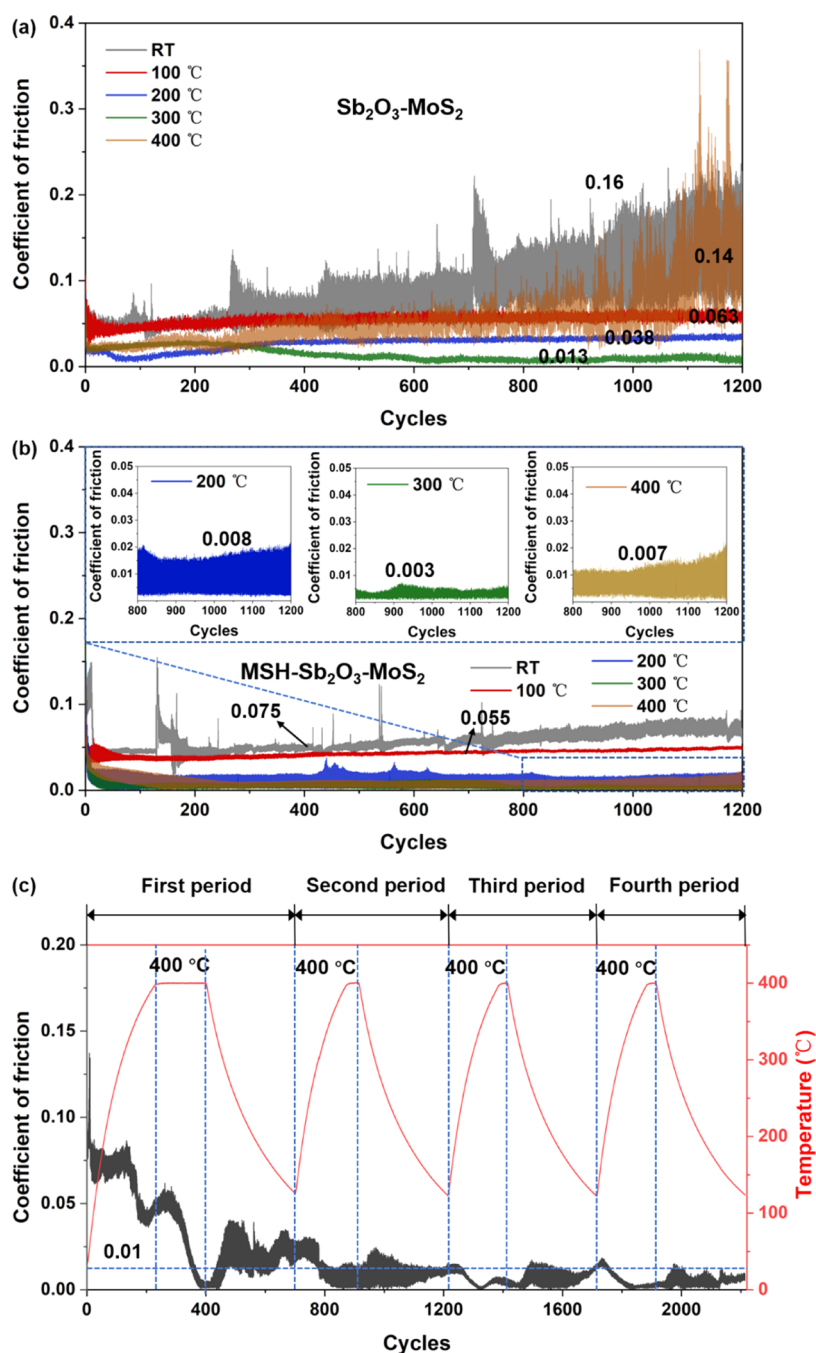
Figure 2. COF as a function of the cycles for (a) Sb$_2$O$_3$−MoS$_2$ and (b) MSH−Sb$_2$O$_3$−MoS$_2$ composite coatings tested at different temperatures. The three illustrations in (b) show the COF values of the MSH−Sb$_2$O$_3$−MoS$_2$ composite coating at 200, 300, and 400 °C. (c) COF evolutions of the MSH−Sb$_2$O$_3$−MoS$_2$ composite coating at variational temperatures between RT and 400 °C.

friction behavior of the MoS$_2$-based composite coatings at high temperatures (200−400 °C), thus offering a novel intrinsic lubrication mechanism for application in tribological systems.

2. EXPERIMENTAL PROCEDURE

2.1. Coatings. The MSH−Sb$_2$O$_3$−MoS$_2$ composite coating was prepared by sequentially burnishing powders of Sb$_2$O$_3$ (0.01 g, AR,

99.5%, supplied by Shanghai Aladdin Bio-Chem Technology Co., Ltd, with an average size of 0.3 μm), MoS$_2$ (0.003 g, AR, 98%, supplied by Shanghai Aladdin Bio-Chem Technology Co., Ltd, with a thickness of approximately 500 nm and an average size of 3 μm), and MSH (0.003 g) onto a polished copper substrate surface (roughness was approximately 0.013 μm, as shown in Figure S1a) using a lint-free cloth. Copper-based materials have been increasingly used in rocket engines owing to their oxygen compatibility and high electrical

conductivity and thermal conductivity; thus, copper was chosen as the coating substrate material. In addition, the X-ray photoelectron spectroscopy (XPS, Krotas AXIS SUPRA) survey spectrum of the copper substrate is analyzed to detect its chemistry composition (57−60% copper and 39−42% zinc; Figure S2). The rotation speed and load changed during the burnishing process in the range of 10−100 rpm and 1−10 N, respectively, to obtain an evenly distributed MSH−Sb_2O_3−MoS_2 composite layer, as shown in Figure S3. The roughness of the as-prepared MSH−Sb_2O_3−MoS_2 composite coatings was approximately 0.258 μm (Figure S1b). The MSH nanomaterials were hydrothermally synthesized at 200 °C and 1.6 MPa for 12 h (a schematic diagram of this nanomaterial synthesis is provided in Figure 1a). More coating preparation details and the specific synthesis details and characteristics of MSH, including the morphology and crystal structure are available in our earlier studies.[33,42,43] The coatings of Sb_2O_3, MSH−Sb_2O_3, and Sb_2O_3−MoS_2, as the comparative test samples, were also prepared using the same burnishing method.

2.2. Tribological Tests. The tribological behavior of the MSH−Sb_2O_3−MoS_2 composite coating and the baseline Sb_2O_3, MSH−Sb_2O_3, and Sb_2O_3−MoS_2 coatings were characterized in an open-air system using a ball-on-disk tribometer with a high-temperature capability (Rtec MFT-3000). Silicon nitride (Si_3N_4) balls with a diameter of 6 mm and roughness of ∼10−20 nm were used as the counterparts. Before the tests, the Si_3N_4 balls were ultrasonically cleaned with acetone and isopropyl alcohol. The tests were performed at temperatures ranging from room temperature (termed as RT in the following text, varied at 17−25 °C) to 100, 200, 300, and 400 °C, in a unidirectional rotational mode at 10 rpm, wear track radius of 4−9 mm (corresponding to linear speeds of 4.2−9.4 mm/s), and an applied load of 0.5 N (corresponding to a maximum Hertzian contact pressure of 430 MPa). The same rotational radii were used under the same test temperature for these four types of coatings, and the variations in the linear speed within this range did not affect the results. For the high-temperature test, the samples were kept at the target temperature for at least 15 min before testing. All experiments were repeated at least three times.

2.3. Characterization. Scanning electron microscopy (SEM, Hitachi SU 8020), transmission electron microscopy (TEM, FEI Technai JEM F200) equipped with energy-dispersive X-ray spectroscopy (EDS) and high-angle annular dark-field (HAADF), Raman spectroscopy (LabRAM HR Evolution, laser wavelength of 532 nm), and white light interferometry (Zygo New View 8300) were employed to detect the morphologies, elemental distributions, structures, and roughness of the as-burnished and tested MSH−MoS_2−Sb_2O_3 composite coatings, respectively. The cross-sectional specimens for TEM were prepared using a focused ion beam (FIB) equipped with SEM to cut and lift off the sample from the wear track. A nanoindentation tester (Berkovich B-T56) was used to obtain the mechanical properties of the coatings, as shown in Table 1 and Figure S4. For this characterization, a three-sided pyramidal diamond indenter with a diameter of 50 nm was used while applying a maximum load of 10 Mn, with linear loading and unloading rates of 20 mN/min. The acquisition rate during the dynamic loading process was 10 Hz, and the indenter remained for 5 s after loading. The Raman detection processes were conducted under a laser light source of visible photons at 532 nm, excitation source energy of 10 mW, and scan range of 120−1000 cm^{-1}.

SEM (Hitachi SU 8020) was used to detect the morphology of the hydrothermally synthesized MSH nanomaterials. To further explore the macroscale superlubricity of the MSH−Sb_2O_3−MoS_2 composite coating, the initial MSH powders were characterized using differential scanning calorimetry/thermogravimetry (DSC−TG, STA 449F3) and high-temperature X-ray diffraction (XRD, Bruker D8 ADVANCE) analyses. The DSC−TG analysis was performed at 30−1000 °C and a heating rate of 10 °C/min in a nitrogen atmosphere. The XRD characterization was performed with a Cu Kα X-ray source (wavelength 0.154 nm) at a diffraction 2θ range of 8−80° changed at a step-scan rate of 4°/min and at various temperatures (at RT, 100, 200, 300, 400, 600, and 800 °C).

3. RESULTS AND DISCUSSION

3.1. Coating Analyses. The hydrothermally synthesized MSH nanopowders used in this study had a slightly curled lamellar morphology with an average particle diameter of approximately 50 nm (Figure 1b).[42] The MSH nanopowders were composed of Si−O tetrahedral sheets, Mg−O/OH octahedral sheets, and adsorbent water molecules (Figure 1c), which generally belong to the layered silicate material. Although Sb_2O_3, MoS_2, and MSH powders were regularly burnished onto the copper substrate, their representative antimony, molybdenum, and magnesium elements were staggered in an accumulated island morphology, as shown in Figures S1b and S3. The coating cross-sectional morphology and the corresponding elemental distribution maps, as shown in Figures 1d and S5, indicate Sb_2O_3-, MoS_2-, and MSH-producing layers in the burnished order (Sb_2O_3 and MSH are located at the bottommost and topmost layers of the coating, respectively). The thickness of the MSH−Sb_2O_3−MoS_2 composite coating was approximately 200 nm; however, this may vary depending on the microscale region for the FIB cross section and the island-like distribution of the coating of the substrate surface. At present, there are mainly two methods to analyzing the coating thickness including the cross-sectional detection by SEM or TEM, the etching elemental detection by XPS or time-of-flight secondary-ion mass spectrometry. Although accurate coating thickness can be obtained, it is limited by high cost, low efficiency, and micron-scale detection, and a more statistically significant manner might be needed. Additionally, given the micron-scale level of EDS detection depth and the nanometer level of the coating thickness, the copper element distribution was observed, as shown in Figure S3.

3.2. Tribological Results. The tribological performances of the coatings were characterized under various temperature conditions. Figure 2a,b shows the coefficient of friction (COF) results for the Sb_2O_3−MoS_2 and MSH−Sb_2O_3−MoS_2 composite coatings tested at different temperatures in an open-air system. In comparison to the stable COFs of 0.16, 0.063, 0.038, 0.013, and 0.14 corresponding to the Sb_2O_3−MoS_2 composite coating at RT, 100, 200, 300, and 400 °C, respectively, those of the MSH−Sb_2O_3−MoS_2 composite coating reduce to 0.075, 0.055, 0.008, 0.003, and 0.007, respectively. Meanwhile, the friction reduction stability significantly improved. When the test temperature was increased to 200 °C or above, the COF values for the MSH−Sb_2O_3−MoS_2 composite coating almost immediately decreased to below 0.01 within 100 revolutions, entering the superlubricity regime[43−45] (observed in the three illustrations of Figure 2b). Notably, for the Sb_2O_3−MoS_2 composite coating, the 300 °C test resulted in a relatively low friction (the COF value reached approximately 0.013) after 600 revolutions, proving the excellent synergistic friction reduction performances of Sb_2O_3 and MoS_2.[33] Nevertheless, the lubricant phase of MoS_2 in Sb_2O_3−MoS_2 could gradually be oxidized in an open high-temperature environment and lose its lubricant effects,[1,2] which could also be predicted from the relatively drastic COF fluctuation, as shown in Figure 2a. A further increase in the temperature up to 400 °C showed a decrease in the COF of the Sb_2O_3−MoS_2 composite coating; however, the low-friction behavior did not last long, and the COF increased after 1000 revolutions.
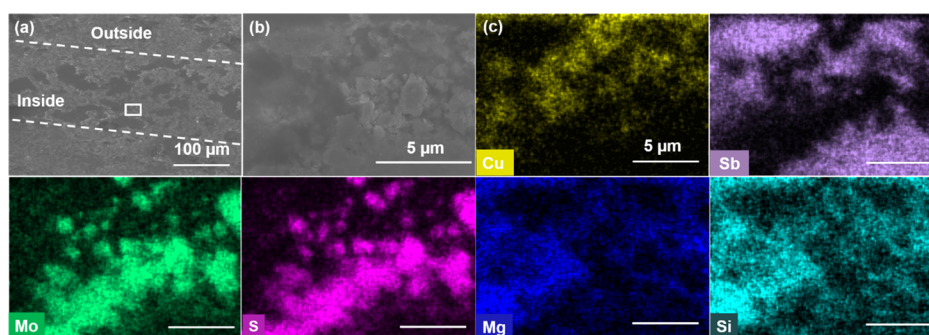
Figure 3. (a) SEM, (b) enlarged SEM morphologies, and (c) elemental distributions inside the wear track of the MSH−Sb$_2$O$_3$−MoS$_2$ composite coating tested at 400 °C. Panel (b) corresponds to the morphology of the frame region in (a). The scale bars in the elemental distribution maps are 5 μm.
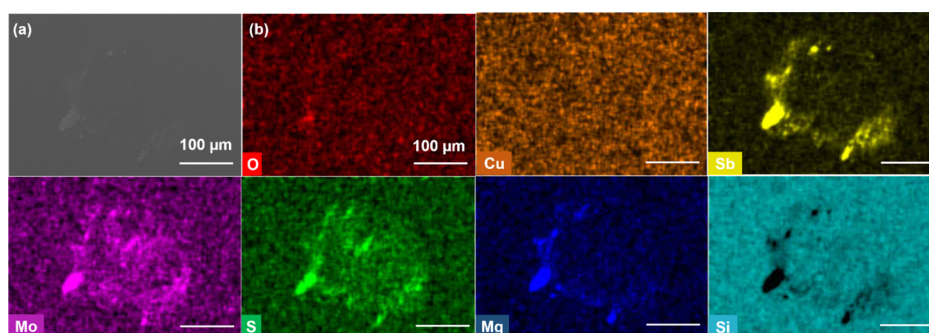
Figure 4. (a) SEM morphology and (b) elemental distributions of the wear scar on the Si$_3$N$_4$ ball sample tested at 400 °C. Because the silicon content in the transfer film is lower than that in the Si$_3$N$_4$ sample, the result shown in (b) cannot be used to characterize the distribution of the transferred silicon. The scale bars in the elemental distribution maps are 100 μm.

We further tested the tribological performance of the Sb$_2$O$_3$ and MSH−Sb$_2$O$_3$ coatings to verify the contributions of MoS$_2$ and Sb$_2$O$_3$ to the low friction of the MSH−Sb$_2$O$_3$−MoS$_2$ composite coating at different temperatures (Figure S6). When the temperature changed from RT to 100, 200, and 300 °C, the COFs of the Sb$_2$O$_3$ coating increased from 0.4 to approximately 0.45, 0.5, and 0.6, respectively (Figure S6a). Notably, as the temperature increased to 400 °C, the friction of the Sb$_2$O$_3$ coating decreased at the beginning of the test and reached a COF value of approximately 0.02 after 200 revolutions; however, it failed after 650 revolutions. The MSH−Sb$_2$O$_3$ composite coating also demonstrated sensitivity to the testing temperature conditions, as shown in Figure S6b. The variations in the testing temperatures for MSH−Sb$_2$O$_3$ from RT up to 100 and 200 °C resulted in stable COFs of 0.20, 0.22, and 0.49, respectively, without any signs of coating failure indications up to 1200 revolutions. As the temperature increased further to 300 and 400 °C, Sb$_2$O$_3$ and MSH exhibited similar synergistic friction reduction effects, that is, the COFs gradually decreased, reaching a stable low friction (COFs are approximately 0.06 and 0.03) after 900 and 600 revolutions, respectively.

To further test the temperature sensitivity in relation to the friction behavior of the MSH−Sb$_2$O$_3$−MoS$_2$ composite coating, we continuously monitored the changes in the COF while alternating the test temperature from RT to 400 °C and to approximately 120 °C. The temperature reduction from 400 °C to RT was difficult to control because of the cooling time limitation, and we termed the above process as RT−400 °C−RT in the following text for simplicity. As shown in Figure 2c, the entire experimental process was divided into four periods

according to the RT−400 °C−RT variation. When the temperature went up from RT to 400 °C in the first period (corresponding to 0−200 revolutions), the COF of the MSH−Sb$_2$O$_3$−MoS$_2$ composite coating first reduced to approximately 0.07. Afterward, it remained stable for a short duration and finally reached approximately 0.05. Once the temperature reached 400 °C, the COF dropped rapidly and entered the superlubricity regime (changed from 0.05 to 0.003) within 100 revolutions. Subsequently, the COF slightly increased as the temperature decreased, and thereafter, it remained at approximately 0.025 until the second period began. During the subsequent three temperature variation periods, the COF tendencies of the MSH−Sb$_2$O$_3$−MoS$_2$ composite coating were consistent with those in the first period. However, the COF value of the composite coating continuously remained below 0.01, regardless of the temperature change in RT−400 °C−RT. That is, after the full temperature variation experiment, the COF of the coatings was not influenced by temperature, and it was possible to achieve superlubricity over a wide temperature range.

Figures 3 and 4 display the morphologies and the corresponding elemental distributions of the MSH−Sb$_2$O$_3$−MoS$_2$ composite coating and the Si$_3$N$_4$ counterpart tested at 400 °C, respectively. To make the Si$_3$N$_4$ ball electrically conductive during the SEM and EDS detection processes, the spherical crown with the wear scar was sprayed by a Pt coating. EDS elemental maps inside the wear track (Figure 3) indicated the presence of copper, antimony, molybdenum, sulfur, magnesium, and silicon, suggesting that the MSH−Sb$_2$O$_3$−MoS$_2$ composite coating was barely consumed, or the Sb$_2$O$_3$ and MoS$_2$ lubricant phases were not pushed out of the contact

regions after 1200 revolutions. Additionally, by observing the enlarged morphology shown in Figure 3b and combining it with the elemental maps shown in Figure 3c–h, Sb_2O_3 could be seen to exist mostly in a fragmented form, whereas MSH mostly existed in a continuous film form. This may provide substantial evidence for the more likely film formation and film shear capabilities of MSH at high temperatures. For the Si_3N_4 counterpart, there was no obvious sign of wear; instead, large amounts of Sb, Mo, S, and Mg indicated material transfer from the MSH–Sb_2O_3–MoS_2 composite coating surface (Figure 4), indicating that the formation of a transfer film is one of the reasons for the observed macroscale superlubricity. The SEM morphologies and elemental distributions of other friction pairs tested at RT (Figures S7 and S8), 100 °C (Figures S9 and S10), 200 °C (Figures S11 and S12), and 300 °C (Figures S13 and S14) were similar to those tested at 400 °C. Therefore, it can be concluded that the MSH–Sb_2O_3–MoS_2 composite coating exhibited a similar transfer film formation mechanism with changes in the temperature from RT to 400 °C.

The phase evolutions of the MSH–Sb_2O_3–MoS_2 composite coating that occurred as a consequence of the tribological tests at different temperatures were analyzed by collecting Raman spectra during the test wear tracks (Figure 5). MSH (at
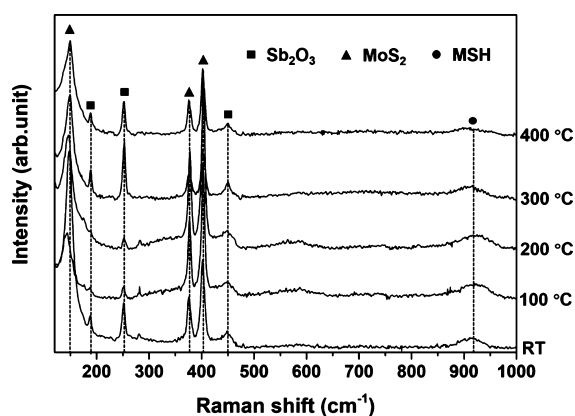

Figure 5. Raman spectra from the wear track of the MSH–Sb_2O_3–MoS_2 composite coating tested at different temperatures. The Raman spectra were acquired from 120 to 1000 cm^{-1} with a 532 nm excitation.

approximately 925 cm^{-1} corresponding to the oscillation of metal–ligand bonds),[44] MoS_2 (at approximately 145, 377, and 404 cm^{-1} corresponding to the S–Mo–S plane vibrational breathing mode of E_{2g} and A_{1g} symmetry),[35,46] and Sb_2O_3 (at approximately 189, 253, and 449 cm^{-1})[34] phases were detected. The Raman results further confirm that under a contact pressure of 430 MPa applied during the high-temperature friction tests, the coating experienced no obvious damage, whereas the lubrication phases of MSH, Sb_2O_3, and MoS_2 exhibited their original crystal structures. Besides, to further explain the sharp increase of COF values for the Sb_2O_3–MoS_2 composite coating as the temperature was increased to 400 °C, Raman analyses of this coating after the tribological tests at different temperatures were also conducted, as shown in Figure S15. Compared with the peak strength of MoS_2 (at approximately 145, 377, and 404 cm^{-1})[35,46] and Sb_2O_3 (at approximately 189, 253, and 449 cm^{-1})[34] inside the wear track tested at temperatures of 100, 200, and 300 °C, that obtained at temperatures of RT and 400 °C decreased sharply.

This is consistent with the friction test results shown in Figure 2 that the Sb_2O_3–MoS_2 composite coating failed after 1200 revolutions at RT and 400 °C.

The cross-sectional TEM and HAADF images in Figures 6 and S16 confirm that the MSH–Sb_2O_3–MoS_2 composite
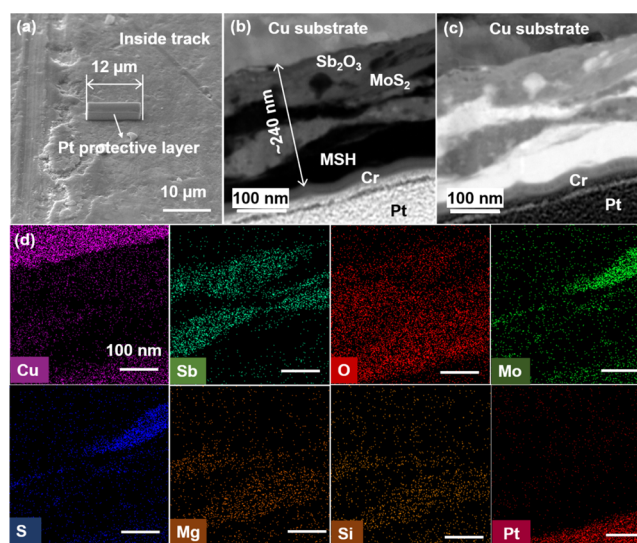

Figure 6. (a) Position of the cross-sectional TEM sample in the FIB preparation process, and the cross-sectional (b) TEM image, (c) HAADF image, and (d) elemental distributions of the MSH–Sb_2O_3–MoS_2 composite coating tested at 400 °C. The scale bars in the elemental distribution maps are 100 nm. Chromium and platinum protective layers were deposited to protect the coating from damage during the TEM specimen preparation. In comparison to the original detection position, there might be some TEM detection drift.

coating was not removed from the sliding interface and did not experience any significant structural transformation after 1200 revolutions of high-temperature sliding, which is consistent with the morphology and elemental distribution analysis shown in Figure 3 and the wear track roughness analysis in Figure S17, that is, the coating after the tribological test at 400 °C still had a layered structure with a thickness of 240–250 nm. This relatively high thickness might be caused by the inaccuracy generated by the FIB microscale region and the coating island-like distribution. This further confirms that the coating was almost not consumed before and after the test. Sb_2O_3 was distributed in the bottommost layer of the coatings closer to the copper substrate; meanwhile, MSH appeared in the topmost layer with depressively scattered MoS_2 (which is shown more distinctly in Figure S16b–d) dominating the macroscale superlubricity.

4. DISCUSSION

Our results indicate that the combination of hydrothermally synthesized MSH, MoS_2, and Sb_2O_3 demonstrated excellent synergistic friction reduction performance and enabled the realization of macroscale superlubricity under high-temperature conditions of 200–400 °C according to the MSH–Sb_2O_3–MoS_2 composite coating's COF evolution, as shown in Figure 2. Considering that the wear-enhancing mechanisms of MoS_2 coatings and Sb_2O_3-containing MoS_2 composite coatings are relatively well known,[1,2,21,29−38] the following discussion will focus on the MSH lubricant phase and its synergistic mechanism when combined with MoS_2 and Sb_2O_3.
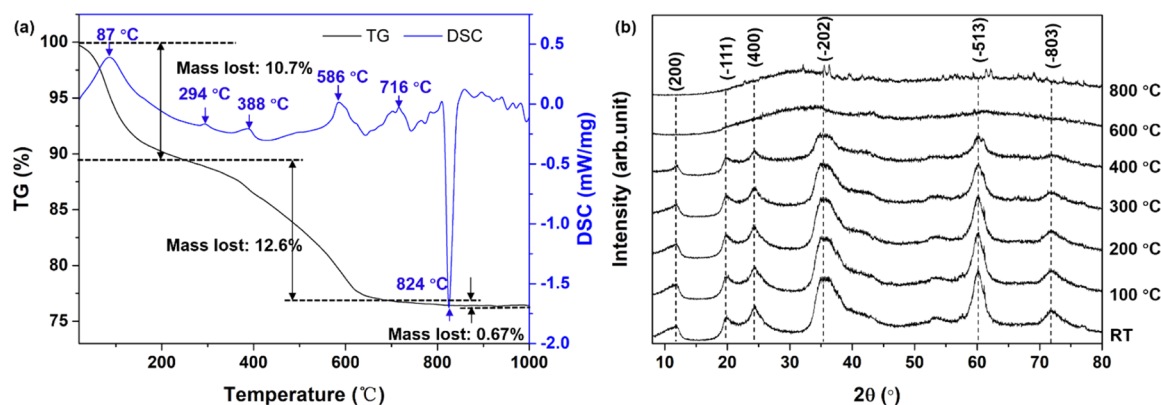
Figure 7. (a) DSC−TG curves and (b) high-temperature XRD patterns of the hydrothermally synthesized MSH nanomaterials.

The DSC−TG curves and high-temperature XRD patterns were characterized to explore the MSH crystal structure evolution as a function of temperature, as shown in Figure 7a,b. As the temperature increased from RT to approximately 200 °C, the first weightless platform corresponding to the loss weight percentage (10.7%) of interlayer absorbent water in the MSH crystal structure (shown in Figure 1b) appeared. Combined with the DSC endothermic peak, these absorbent water molecules evaporated in large quantities near 87 °C. Combined with the experimental results, shown in Figure 2b, the COF of the MSH−Sb_2O_3−MoS_2 composite coating tested at 100 °C decreased from 0.075 to 0.065 compared with that tested at room temperature. Therefore, it is concluded that the absorbent water in MSH hindered the interlaminar slip to some extent. This can also be speculated from the COF evolution of the coating at the temperature of 200 °C starting to enter superlubricity. Subsequently, the MSH nanomaterial weight continuously decreased until the second weightless platform (12.6%) emerged at a temperature range of 250−640 °C, which corresponded to the destruction of structural water (hydroxyl group in Mg−O/OH octahedral sheets), which somehow means the destruction of the MSH crystal structure, and residual interlayer adsorbent water in MSH. With the temperature increase, the loss of structural water is gradually serious, contributing to an obvious increase of COF when the temperature was increased from 300 to 400 °C (Figure 2b). A small and wide endothermic peak emerged in the DSC curve at approximately 586 °C. Meanwhile, the crystal structure of MSH was destroyed, and new phases were generated. When the temperature sequentially increased to 824 °C, the DSC curve showed a strong and sharp exothermic peak. Under these temperature conditions, the crystal structure of MSH was destroyed, and its mass did not decrease significantly with the continuous increase in temperature, remaining at 76.03% of the original weight. However, at this time, MSH decomposed into other substances. These conclusions can also be obtained by the high-temperature XRD characterization shown below.

As shown in Figure 7b, the diffraction peaks in the high-temperature XRD patterns of the MSH nanomaterials showed no obvious change with temperature from RT to 400 °C and appeared at 2θ = 11.9, 19.9, 24.4, 35.3, 60.3 and 71.9°, which largely correspond with the crystallographic planes (200), (−111), (400), (−202), (−513), and (−803) of chrysotile minerals (PDF 02-0094).[42] This demonstrates that the hydrothermally synthesized MSH did not decompose during the high-temperature friction tests; it maintained the same crystal structure but with different amounts of absorbed water

or structural water (speculated from Figure 7a). When the temperature increases to 600 °C, the crystal diffraction peaks of MSH disappeared, indicating that its structure has been destroyed. Sequentially, with the temperature continued to rise to 800 °C, some new peaks appeared, which demonstrated that MSH had been transformed to other substances. Therefore, the peaks in the temperature range of 250−640 °C in Figure 7a appeared not only by the destruction of structural water but also by the destruction of the MSH structure. Additionally, no peak corresponding to the residual magnesium hydroxide ($Mg(OH)_2$) appeared by the incomplete hydrothermal reaction.[33−35] This was due to the improvement of the synthesis process; that is, the complete hydrolysis of silicon oxide (SiO_2) occurred first.

To further reveal the influence of the MSH interlayer absorbent water and structural water on the macroscale superlubricity of the MSH−Sb_2O_3−MoS_2 composite coating at high temperatures, it was further dried at 400 °C for 1 h while ensuring the crystal structure. Subsequently, the MSH−Sb_2O_3−MoS_2 composite coating was prepared using the same burnishing process. The tribological test conditions were consistent with those shown in Experimental Procedure, specifically, the temperatures of RT, 100, 200, 300, and 400 °C, a rotational speed of 10 rpm, and an applied load of 0.5 N. As shown in Figure 8, the maximized removal of the MSH interlayer absorbent water and structural water can effectively reduce the COF values of the composite coating at all test temperatures (RT−400 °C). The test temperatures of RT,
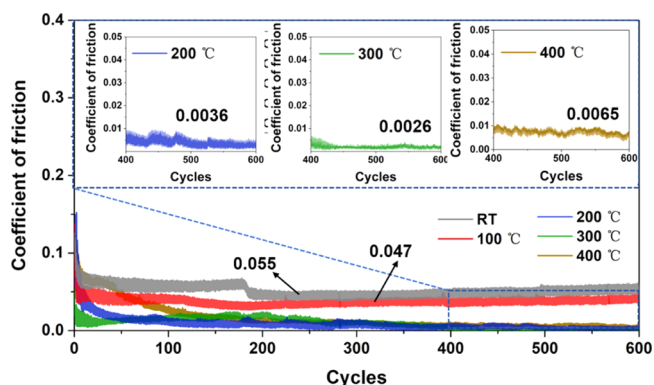
Figure 8. COF evolutions of the MSH−Sb_2O_3−MoS_2 composite coating, in which the MSH lubricant phase was insulated at 400 °C for 1 h. The three illustrations in Figure 8 show COF values more clearly at 200, 300, and 400 °C.
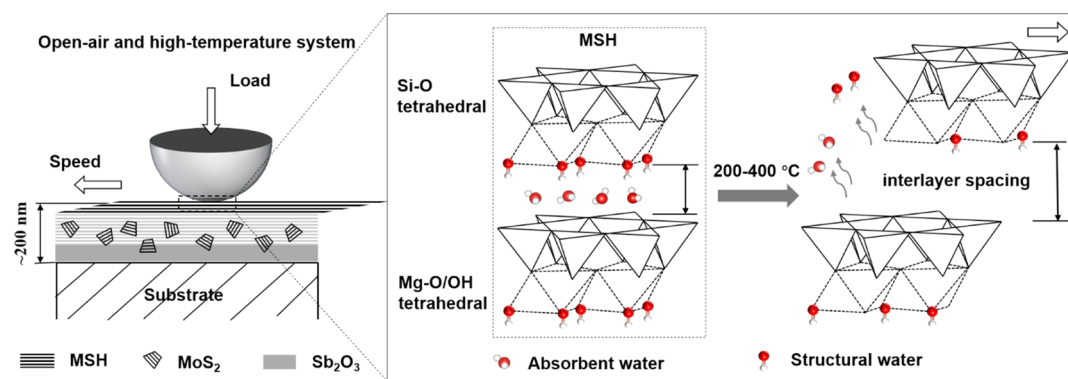
Figure 9. Schematic of the macroscale superlubricity accomplished by the MSH−Sb$_2$O$_3$−MoS$_2$ composite coatings at high temperatures.

100, 200, 300, and 400 °C corresponded to the COFs of 0.055, 0.047, 0.0036, 0.0026, and 0.0065, respectively, which is also consistent with the variation trend of COFs with the test temperature. Therefore, it can be inferred that in addition to the influence of interlayer absorbent water on the tribological properties of the composite coating, the test temperature also plays a significant role in promoting the release of residual absorbent water and intralayer structural water from MSH, thus having an effect on the friction process. The absorbent water of MSH has no essential effect on the high-temperature antifriction performance of the coating; however, its removal can improve MSH-based coating's tribological performance to a certain extent.

The mechanisms of the high-temperature superlubricity accomplished by the MSH−Sb$_2$O$_3$−MoS$_2$ composite coating are speculated in Figure 9, according to the frictional and characterization results. The MSH−Sb$_2$O$_3$−MoS$_2$ composite coating was composed of MSH in the topmost layer, Sb$_2$O$_3$ in the bottommost layer, and MoS$_2$ in a random distribution. It also showed no obvious structural variation and lubricant phase transformation in an open-air environment under varied temperature conditions (from RT to 400 °C), at a contact pressure of 430 MPa, and linear speeds of 4.2−9.4 mm/s. MSH is a 1:1 layered trioctahedral magnesium silicate and consists of oxygen-containing Si−O tetrahedral sheets and hydroxyl group-containing Mg−O/OH octahedral sheets connected via van der Waals forces and hydrogen bonds which are much weaker than ionic bonds and covalent bonds in the basic units.[42] Because of this weak bonding force between the layers, under the condition of a certain pressure and temperature, MSH easily experienced cleaving and slipping along the bending direction. Although MSH is theoretically electricity-saturated and it is difficult for water molecules to enter between the basic structural units, there is still a certain amount of adsorption water (approximately 10.7% shown in Figure 7a) due to sodium (Na) substitution and insufficient drying during the hydrothermal reaction process. The temperature increases from RT to the limit temperature of the MSH crystal structure (higher than 400 °C, as shown in Figure 7b), contributing to the gradual release of adsorption water and structural water (hydrogen bonds in Mg−O/OH octahedral sheets), causing the layer spacing to increase, as presented in Figure 9. This temperature sensitivity facilitated MSH shearing along the direction of the bending plane, and therefore, low-friction behavior was observed, which was verified by the frictional test results of the MSH−Sb$_2$O$_3$ composite coating, as shown in Figure S6. In addition to the

high-temperature shear susceptibility of MSH itself, Sb$_2$O$_3$ and MoS$_2$ simultaneously exert a synergistic effect on the superlubricity process, providing a relatively strong basal support and a relatively easy shearing support, respectively, for the low-friction MSH lubricants.

5. CONCLUSIONS

In conclusion, we have introduced a new solid lubricant phase of hydrothermally synthesized MSH nanomaterial and used it as one of the lubricant phases to design an MSH−Sb$_2$O$_3$−MoS$_2$ composite coating by a burnishing method. While the friction remained relatively high at RT and 100 °C, our analysis indicated the macroscale superlubricity of the coating when tested at elevated temperatures from 200 to 400 °C. The wear track analysis and MSH characteristics suggested that the origin of such high-temperature behavior is an easy shearing property of MSH at high temperature, which is enabled by the missing adsorption water between the basic units and the increase in interlayer spacing. Meanwhile, Sb$_2$O$_3$ and MoS$_2$ have a synergistic effect, providing a relatively strong and adhesive layer support for the low-friction lubricants. Our results provide new insights into high-temperature lubrication systems that can be easily sheared by supplying lubricant materials to the sliding contacts through the burnishing process.

◼ ASSOCIATED CONTENT

ⓢ Supporting Information

The Supporting Information is available free of charge at https://pubs.acs.org/doi/10.1021/acsanm.1c01104.

> Detailed roughness characteristics and mechanical properties of polished copper substrate and burnished coatings, tribological test results of Sb$_2$O$_3$ and MSH−Sb$_2$O$_3$ coatings at high temperatures, and coating characterization data from SEM, TEM, and EDS (PDF)

◼ AUTHOR INFORMATION

Corresponding Author

Yu Tian − *State Key Laboratory of Tribology, School of Mechanical Engineering, Tsinghua University, Beijing 100084, P. R. China;* ⓘ orcid.org/0000-0001-7742-5611; Email: tianyu@mail.tsinghua.edu.cn

Authors

Bin Wang − *State Key Laboratory of Tribology, School of Mechanical Engineering, Tsinghua University, Beijing 100084, P. R. China*

Kai Gao − *State Key Laboratory of Tribology, School of Mechanical Engineering, Tsinghua University, Beijing 100084, P. R. China*

Qiuying Chang − *School of Mechanical, Electronic and Control Engineering, Beijing Jiaotong University, Beijing 100044, P. R. China;* ⓘ orcid.org/0000-0002-2166-8187

Diana Berman − *Department of Materials Science and Engineering, University of North Texas, Denton, Texas 76203, United States;* ⓘ orcid.org/0000-0002-9320-9772

Complete contact information is available at:
https://pubs.acs.org/10.1021/acsanm.1c01104

Notes

The authors declare no competing financial interest.

■ REFERENCES

(1) Lince, J. R. Effect application of solid lubricants in spacecraft mechanisms. *Lubricants* **2020**, *8*, 74.

(2) Muratore, C.; Voevodin, A. A. Chameleon coatings: adaptive surface to reduce friction and wear in extreme environments. *Annu. Rev. Mater. Res.* **2009**, *39*, 297−324.

(3) Donnet, C.; Martin, J. M.; Le Mogne, T.; Belin, M. Super-low friction of MoS_2 coatings in various environments. *Tribol. Int.* **1996**, *29*, 123−128.

(4) Rapoport, L.; Fleischer, N.; Tenne, R. Applications of WS_2 (MoS_2) inorganic nanotubes and fullerene-like nanoparticles for solid lubrication and for structural nanocomposites. *J. Mater. Chem.* **2005**, *15*, 1782−1788.

(5) Chhowalla, M.; Amaratunga, G. A. J. Thin films of fullerene-like MoS_2 nanoparticles with ultra-low friction and wear. *Nature* **2000**, *407*, 164−167.

(6) Aouadi, S. M.; Gu, J.; Berman, D. Self-healing ceramic coatings that operate in extreme environments: a review. *J. Vac. Sci. Technol., A* **2020**, *38*, 050802.

(7) Sliney, H. E.; Strom, T. N.; Allen, G. P. Fluoride solid lubricants for extreme temperatures and corrosive environments. *ASLE Trans.* **1965**, *8*, 307−322.

(8) Deadmore, D. L.; Sliney, H. E. Hardness of CaF_2 and BaF_2 solid lubricants at 25 to 670 °C; NASA TM 88979; National Aeronautics and Space Administration, 1987; Vol. *143* (702), pp 1−21.

(9) Grill, A. Tribology of diamondlike carbon and related materials: an updated review. *Surf. Coat. Technol.* **1997**, *94−95*, 507−513.

(10) Donnet, C. Advanced solid lubricant coatings for high vacuum environments. *Surf. Coat. Technol.* **1996**, *80*, 151−156.

(11) Zabinski, J. S.; Donley, M. S.; Dyhouse, V. J.; McDevitt, N. T. Chemical and tribological characterization of PbO-MoS_2 films grown by pulsed laser deposition. *Thin Solid Films* **1992**, *214*, 156−163.

(12) Zabinski, J. S.; Day, A. E.; Donley, M. S.; Dellacorte, C. D.; McDevitt, N. T. Synthesis and characterization of a high-temperature oxide lubricant. *J. Mater. Sci.* **1996**, *29*, 5875−5879.

(13) Prasad, S. V.; McDevitt, N. T.; Zabinski, J. S. Tribology of tungsten disulfide-nanocrystalline zinc oxide adaptive lubricant films ambient to 500 °C. *Wear* **2000**, *237*, 186−196.

(14) Wagner, R. C.; Sliney, H. E. Effects of silver and group II fluorides addition to plasma sprayed chromium carbide high temperature solid lubricant for foil gas bearings to 650 °C. NASA TM 86895, *Annual Meeting of the American Society of Lubrication Engineers*, 1985.

(15) Voevodin, A. A.; Fitz, T. A.; Hu, J. J.; Zabinski, J. S. Nanocomposite tribological coatings with "chameleon" friction surface adaptation. *J. Vac. Sci. Technol., A* **2002**, *20*, 1434−1444.

(16) Baker, C. C.; Hu, J. J.; Voevodin, A. A. Preparation of Al_2O_3/ DLC/Au/MoS_2 chameleon coatings for space and ambient environments. *Surf. Coat. Technol.* **2006**, *201*, 4224−4229.

(17) Voevodin, A. A.; O'Neill, J. P.; Zabinski, J. S. WC/DLC/WS_2 nanocomposite coatings for aerospace tribology. *Tribol. Lett.* **1999**, *6*, 75−78.

(18) Rosenkranz, A.; Costa, H. L.; Baykara, M. Z.; Martini, A. Synergetic effects of surface texturing and solid lubricants to tailor friction and wear-A review. *Tribol. Int.* **2021**, *155*, 106792.

(19) Martin, J. M.; Pascal, H.; Donnet, C.; Le Mogne, T.; Loubet, J. L.; Epicier, T. Superlubricity of MoS_2: crystal orientation mechanisms. *Surf. Coat. Technol.* **1994**, *68−69*, 427−432.

(20) Spirko, J. A.; Neiman, M. L.; Oelker, A. M.; Klier, K. Electronic structure and reactivity of defect MoS_2. *Surf. Sci.* **2003**, *542*, 192−204.

(21) Zabinski, J. S.; Donley, M. S.; Walck, S. D.; Schneider, T. R.; Mcdevitt, N. T. The effects of dopants on the chemistry and tribology of sputter-deposited MoS_2 films. *Tribol. Trans.* **1995**, *38*, 894−904.

(22) Nainaparampil, J. J.; Phani, A. R.; Krzanowski, J. E.; Zabinski, J. S. Pulsed laser-ablated MoS_2-Al films: friction and wear in humid conditions. *Surf. Coat. Technol.* **2004**, *187*, 326−335.

(23) Lince, J. R. Tribology of co-sputtered nanocomposite Au/MoS_2 solid lubricant films over a wide contact stress range. *Tribol. Lett.* **2004**, *17*, 419−428.

(24) Lu, X.; Yan, M.; Yan, Z.; Chen, W.; Sui, X.; Hao, J.; Liu, W. Exploring the atmospheric tribological properties of MoS2-(Cr, Nb, Ti, Al, V) composite coatings by high throughout preparation method. *Tribol. Int.* **2021**, *156*, 106844.

(25) Li, L.; Lu, Z.; Pu, J.; Hou, B. Investigating the tribological and corrosive properties of MoS2/Zr coatings with the continuous evolution of structure for high-humidity application. *Appl. Surf. Sci.* **2021**, *541*, 148453.

(26) Han, C. H.; Li, G. L.; Ma, G. Z.; Shi, J. D.; Liu, Y. F.; Li, Z. Preparation and tribological properties of Mo/MoS2-Pb-PbS composite films. *Surf. Coat. Technol.* **2021**, *405*, 126625.

(27) Gaardos, M. N. The synergistic effects of graphite on the friction and wear of MoS_2 films in air. *Tribol. Trans.* **1988**, *31*, 214−227.

(28) Li, B.; Xv, W.; Liu, P.; Huang, D.; Zhou, X.; Zhao, R.; Li, S.; Liu, Q.; Jiang, X. Novel green lubricated materials: Aqueous PAI-MoS_2-graphite bonded solid lubricating coating. *Prog. Org. Coat* **2021**, *155*, 106225.

(29) Zabinski, J. S.; Donley, M. S.; McDevitt, N. T. Mechanistic study of the synergism between Sb_2O_3 and MoS_2 lubricant systems using Raman spectroscopy. *Wear* **1993**, *165*, 103−108.

(30) Centers, P. W. The role of oxide and sulfide additions in solid lubricant compacts. *Tribol. Trans.* **1987**, *31*, 149−156.

(31) Lince, J. R.; Loewenthal, S. H.; Clark, C. S. Tribological and chemical effects of long term humid air exposure on sputter-deposited nanocomposite MoS_2 coatings. *Wear* **2019**, *432−433*, 202935.

(32) Hu, J. J.; Bultman, J. E.; Zabinski, J. S. Microstructure and lubrication mechanism of multilayered MoS_2/Sb_2O_3 thin films. *Tribol. Lett.* **2006**, *21*, 169−174.

(33) Zabinski, J. S.; Bultman, J. E.; Sanders, J. H.; Hu, J. J. Multi-environmental lubrication performance and lubrication mechanism of MoS_2/Sb_2O_3/C composite films. *Tribol. Lett.* **2006**, *23*, 155−163.

(34) Shirani, A.; Joy, T.; Rogov, A.; Lin, M.; Yerokhin, A.; Mogonye, J.-E.; Korenyi-Both, A.; Aouadi, S. M.; Voevodin, A. A.; Berman, D. PEO-Chameleon as a potential protective coating on cast aluminum alloys for high-temperature applications. *Surf. Coat. Technol.* **2020**, *397*, 126016.

(35) Lin, M.; Nemcova, A.; Voevodin, A. A.; Korenyi-Both, A.; Liskiewicz, T. W.; Laugel, N.; Matthews, A.; Yerokhin, A. Surface characteristics underpinning fretting wear performance of heavily loaded duplex chameleon/PEO coatings on Al. *Tribol. Int.* **2021**, *154*, 106723.

(36) Scharf, T. W.; Kotula, P. G.; Prasad, S. V. Friction and wear mechanisms in $MoS_2/Sb_2O_3/Au$ nanocomposite coatings. *Acta Mater.* **2010**, *58*, 4100−4109.

(37) Xu, Y.; Xie, M.; Li, Y.; Zhang, G.; Xu, X.; Fan, X.; Sun, Q.; Li, H.; Zhu, M. The effect of Si content on the structure and tribological performance of MoS_2/Si coatings. *Surf. Coat. Technol.* **2020**, *403*, 126362.

(38) Hudec, T.; Roch, T.; Gregor, M.; Orovčík, L.; Mikula, M.; Polcar, T. Tribological behavior of Mo-S-N solid lubricant coatings in vacuum, nitrogen gas and elevated temperatures. *Surf. Coat. Technol.* **2021**, *405*, 126722.

(39) Gao, K.; Chang, Q.; Wang, B.; Zhou, N.; Qing, T. Synthetic magnesium silicate hydroxide nanoparticles coated with carbonaceous shell in subcritical water condition. *Appl. Surf. Sci.* **2018**, *450*, 312−317.

(40) Gao, K.; Chang, Q.; Wang, B.; Zhou, N.; Qing, T. The tribological performances of modified magnesium silicate hydroxide as lubricant additive. *Tribol. Int.* **2018**, *121*, 64−70.

(41) Wang, B.; Chang, Q. Y.; Gao, K. A hydrothermal reacting approach to prepare few-layer graphene from bulk graphite. *Appl. Surf. Sci.* **2019**, *479*, 20−24.

(42) Wang, B.; Chang, Q. Y.; Gao, K.; Fang, H. R.; Qing, T.; Zhou, N. N. The synthesis of magnesium silicate hydroxide with different morphologies and the comparison of their tribological properties. *Tribol. Int.* **2018**, *119*, 672−679.

(43) Gao, K.; Wang, B.; Shirani, A.; Chang, Q.; Berman, D. Macroscale superlubricity accomplished by Sb_2O_3-MSH/C under high temperature. *Front. Chem.* **2021**, *9*, 226.

(44) Berman, D.; Erdemir, A.; Sumant, A. V. Approaches for achieving superlubricity in two dimensional materials. *ACS Nano* **2018**, *12*, 2122−2137.

(45) Martin, J. M.; Erdemir, A. Superlubricity: friction's vanishing act. *Phys. Today* **2018**, *71*, 40−46.

(46) Windom, B. C.; Sawyer, W. G.; Hahn, D. W. A Raman spectroscopic study of MoS_2 and MoO_3: applications to tribological systems. *Tribol. Lett.* **2011**, *42*, 301−310.